




Hermite-scan imaging for differentiating glioblastoma from normal brain: Simulations and *ex vivo* studies for applications in intra-operative tumor identification^{a)}

Manik Kakkar,¹ Jagruti M. Patil,² Vishwas Trivedi,¹ Anushka Yadav,¹ Ratan K. Saha,³  Shilpa Rao,⁴ Vikas Vazhayil,⁵ Hardik J. Pandya,⁶ Anita Mahadevan,⁴ Himanshu Shekhar,¹  and Karla P. Mercado-Shekhar^{2,b)} 

¹Department of Electrical Engineering, Indian Institute of Technology Gandhinagar, Gandhinagar, Gujarat 382355, India

²Department of Biological Sciences and Engineering, Indian Institute of Technology Gandhinagar, Gandhinagar, Gujarat 382355, India

³Department of Applied Sciences, Indian Institute of Information Technology Allahabad, Prayagraj, Uttar Pradesh 211015, India

⁴Department of Neuropathology, National Institute of Mental Health and Neurosciences, Bangalore, Karnataka 560029, India

⁵Department of Neurosurgery, National Institute of Mental Health and Neurosciences, Bangalore, Karnataka 560029, India

⁶Department of Electronic Systems Engineering, Indian Institute of Science, Bangalore, Karnataka 560012, India

ABSTRACT:

Hermite-scan (H-scan) imaging is a tissue characterization technique based on the analysis of raw ultrasound radio frequency (RF) echoes. It matches the RF echoes to Gaussian-weighted Hermite polynomials of various orders to extract information related to scatterer diameter. It provides a color map of large and small scatterers in the red and blue H-scan image channels, respectively. H-scan has been previously reported for characterizing breast, pancreatic, and thyroid tumors. The present work evaluated H-scan imaging to differentiate glioblastoma tumors from normal brain tissue *ex vivo*. First, we conducted 2-D numerical simulations using the k-wave toolbox to assess the performance of parameters derived from H-scan images of acoustic scatterers (15–150 μm diameters) and concentrations (0.2%–1% w/v). We found that the parameter intensity-weighted percentage of red (IWPR) was sensitive to changes in scatterer diameters independent of concentration. Next, we assessed the feasibility of using the IWPR parameter for differentiating glioblastoma and normal brain tissues ($n = 11$ samples per group). The IWPR parameter estimates for normal tissue ($44.1\% \pm 1.4\%$) were significantly different ($p < 0.0001$) from those for glioblastoma ($36.2\% \pm 0.65\%$). These findings advance the development of H-scan imaging for potential use in differentiating glioblastoma tumors from normal brain tissue during resection surgery. © 2023 Acoustical Society of America.

<https://doi.org/10.1121/10.0023952>

(Received 9 July 2023; revised 29 October 2023; accepted 28 November 2023; published online 18 December 2023)

[Editor: Xiaoming Zhang]

Pages: 3833–3841

I. INTRODUCTION

Standard imaging techniques, such as magnetic resonance imaging (MRI) and computed tomography (CT) scans, are ineffective for accurately assessing glioblastoma tumor margins during surgery. The reasons include safety issues of CT, repeatability with MRI, and accuracy of image fusion due to brain shift.^{1,2} Currently, there is a lack of cost-effective intra-operative imaging tools that can accurately identify tumor margins. Fluorescence imaging, intraoperative MRI, and conventional brightness-mode (B-mode) ultrasound have been utilized for this purpose, but they have limitations. Fluorescence imaging has low sensitivity for detecting tumor margins, and intraoperative MRI is expensive and not widely available.¹

Hermite-scan (H-scan) is a tissue classification method in which raw radio frequency (RF) backscattered signals are

matched to various orders of Gaussian-weighted Hermite polynomials that can represent scatterer diameter.^{3,4} H-scan imaging generates color-coded images; wherein large scatterers are represented in the red channel and small scatterers are mapped in the blue channel. Tissues can exhibit packing fraction and cell size variations due to inflammation, edema, and pathological processes. Detecting changes in size, concentration, and resulting scattering properties has long been a goal in medical ultrasound.^{5,6} Unlike tissue characterization techniques, such as backscatter coefficient imaging, spectral feature extraction, and envelope statistical analyses,^{7–10} H-scan does not require calibration of the transducer probe and imaging system. Although H-scan predominantly concentrates on capturing the relative dimensions of acoustic scatterers, taking a qualitative approach, H-scan provides images with higher spatial resolution than those of the kernel-based methods for characterizing tissues.

H-scan imaging has been reported to differentiate normal and cancerous tissue, and assess cancer progression and treatment response.^{11–19} It has been successful in identifying normal, benign, and malignant thyroid and breast tumors *in vivo*,^{14–16,20,21} and distinguishing different types of

^{a)}Part of this work was presented in “Evaluating the feasibility of differentiating glioblastoma and normal brain tissue using H-scan imaging: An *ex vivo* study,” 184th Meeting of the Acoustical Society of America, Chicago, Illinois, USA, May 2023.

^{b)}Email: karlamshekhar@iitgn.ac.in

melanomas in a small animal model.²² Glioblastoma (GBM) is a highly aggressive primary malignant tumor of the central nervous system. Overall survival of patients with GBM is poor, with an average survival of 18 months with maximal therapy. The mainstay of GBM therapy involves maximal and safe surgical resection. Intraoperative ultrasound is an important tool in neurosurgical procedures for delineating tumors from normal brain tissue is well known. However, the resolution of conventional ultrasound imaging makes it difficult to differentiate the boundary between normal and GBM tissue. This is especially true when imaging is done towards the end of surgery when tissue handling, bleeding and residual tumor would appear similar and difficult to differentiate using conventional ultrasound.²³ The high scatterer diameter sensitivity of the H-scan could potentially prove more efficacious for the precision in delineation between tumor and non-tumorous tissue in the central nervous system. This capability would contribute to the overarching objective of achieving maximal, yet safe resection, while ensuring the preservation of function in adjacent brain areas and minimizing associated morbidity. Specialized probes with the H-scan imaging capability will be valuable to delineate tumor and tumor-margins intraoperatively and aid the neurosurgeon to achieve maximal and safe resection to ensure best results for patients with brain tumors.

The goal of this study was twofold. First, to quantify the effect of scatterer diameter and concentration on H-scan images through simulations using the k-wave toolbox in MATLAB.²⁴ We successfully identified an H-scan parameter dependent on the scatterer diameter and independent of the scatterer concentration. We then tested the hypothesis that H-scan imaging can be used to differentiate glioblastoma tumors from normal brain tissue *ex vivo*.

II. METHODS

Hermite polynomials are defined as²⁵

$$H_n(t) = (-1)^n e^{t^2} \frac{d^n}{dt^n} e^{-t^2}, \quad n = 0, 1, 2, \dots; \quad t \in \pm\infty. \quad (1)$$

When $H_n(t)$ is multiplied by $G(t) = e^{-t^2}$, then the polynomials become Gaussian-weighted Hermite (GH) polynomials. The energy of a GH polynomial is defined as

$$E = \int_{-\infty}^{\infty} H_n^2 G^2(t) dt. \quad (2)$$

The GH polynomial is energy-normalized by dividing the GH polynomial by the square root of its energy. Examples of GH polynomials are shown in Fig. 1.

A. Algorithms

1. 2-convolution H-scan algorithm

In the 2-convolution H-scan algorithm, each RF line was convolved parallelly with the energy-normalized GH_2 and GH_8 filters. GH_2 represented the low-frequency components of the backscattered signal and corresponded to the

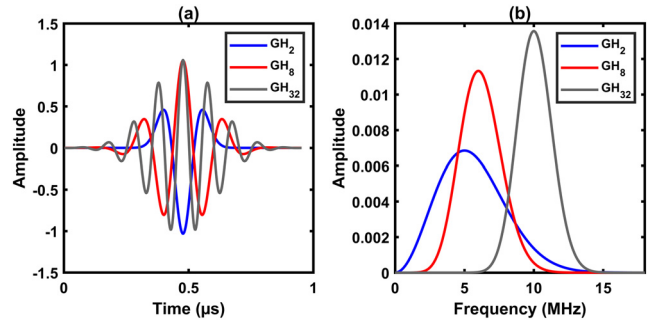


FIG. 1. (Color online) Gaussian-weighted Hermite polynomials of the 2nd, 8th, and 32nd order, i.e., GH_2 , GH_8 , and GH_{32} , respectively, in the (a) time and (b) frequency domain.

red channel, representing larger scatterers. GH_8 corresponded to the high-frequency components and represented the smaller scatterers.^{26–28} The mean intensity of the red channel (MIRC) was computed to estimate the fraction of large scatterers in the tissue.

2. 64-convolution H-scan algorithm

In the 64-convolution H-scan algorithm, each RF line was convolved parallelly with energy-normalized GH kernels of even orders ranging from 2 to 128 (Fig. 2). The peak frequency of each filter was chosen to cover the bandwidth of the received signal. Pseudo-coloring was then applied based on the order of the best-matched (correlation) filter at each pixel.^{4,29–31} Lower-order filters represented relatively larger scatterers and were assigned a red color, while higher-order filters represented relatively smaller scatterers and were assigned a blue color.^{4,27} The color intensity was varied based on the distance of the order value from the midpoint, which is the 64th order. The intensity-weighted percentage of red (IWPR) was computed for each location according to the following equation:

$$IWPR = \frac{\sum_{i \in R} I_i}{\sum_{i \in R} I_i + \sum_{i \in B} I_i} \times 100\%, \quad (3)$$

where I_i is normalized color intensity for every pixel i . The indices, $i \in B$ and $i \in R$, correspond to the red and blue pixels within the ROI, respectively. The IWPR is complementary to

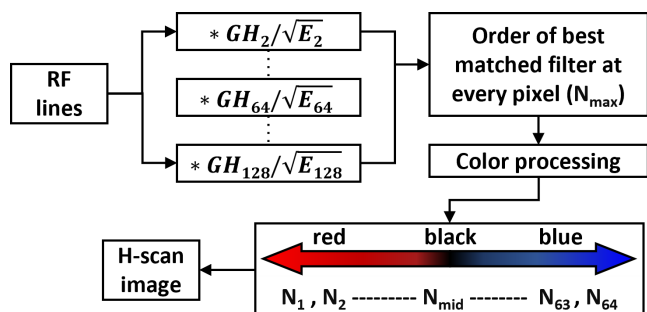


FIG. 2. (Color online) Schematic of the 64-convolution H-scan algorithm.

the intensity-weighted percentage of blue (IWPB), wherein their sum equals 100%.⁴

B. Simulation setup

The k-wave simulation toolbox in MATLAB (R2020b, The MathWorks Inc, Natick, MA) was utilized for this study. The simulated output was the time series RF data generated from linear array imaging. A computer running the Windows operating system with a 64-bit AMD EPYC 730 216-Core Processor [@ 3.00 GHz], 512 GB RAM, and 24 GB VRAM NVIDIA Quadro RTX 6000 was used. The simulations were performed in GPU using the CUDA capability of the k-wave toolbox.

1. Medium

A two-dimensional computational grid was used for all the simulations. The grid had 1024×2048 pixels ($2.5 \mu\text{m}/\text{pixel}$) including a $100 \mu\text{m}$ perfectly matched layer to satisfy the boundary condition. A medium sound speed of 1540 m/s and a density of 1000 kg/m^3 were used. No frequency-dependent attenuation or dispersion of sound was introduced. A total of 27 412 timesteps were taken, each of 256 pico-seconds.

2. Scatterer distribution

Micro-discs composed of polyethylene were simulated as weakly scattering materials and served as an acoustic model of cells in tissue. A sound speed of 1950 m/s and a density of 960 kg/m^3 were assumed for polyethylene. Randomly placed monodispersed and bimodal scatterer diameter distributions were simulated. A 1 mm layer of water was assumed between the transducer and numerical scatterer phantoms (NSPs).

- (a) *Monodispersed scatterer distribution:* Fifty NSPs were created, each with 10 independent and random realizations. These NSPs were generated with five different concentrations (0.2%–1% w/v) and 10 different scatterer diameters (15–150 μm).
- (b) *Bimodal scatterer distribution:* Fifty-five NSPs were created, each with 5 independent and random realizations. These NSPs were generated with five different concentrations (0.2%–1% w/v) using a bimodal mixture of two scatterer diameters: 50 and 90 μm . Eleven different % volume (0%–100%) of 90 μm scatterers were simulated. The NSP for 70% volume of 90 μm scatterers and a total scatterer concentration of 1% w/v is illustrated in Fig. 3(a).

3. Transducer

The transducer source was modelled after an L11-5v linear array (used subsequently in experiments) with an element width of $270 \mu\text{m}$ and a pitch of $300 \mu\text{m}$. A total of 8 elements were active in the RF scan. The F-number was set to 1.2, consistent with the subsequent imaging experiments. The transmit signal was a broadband 1 MPa GH_4 pulse with

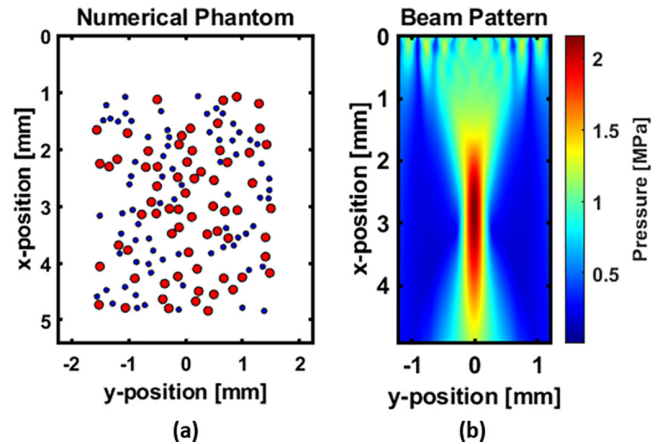


FIG. 3. (Color online) (a) Representative numerical scattering phantom of a bimodal distribution of $50 \mu\text{m}$ and $90 \mu\text{m}$ scatterers. (b) Simulated transducer beam profile.

a central frequency of 7.6 MHz. Eight RF lines were acquired for each NSP. The simulated transducer beam pattern is shown in Fig. 3(b). To assess robustness, a Gaussian noise with a signal-to-noise ratio of 20 dB was added to all recorded RF lines.

C. Ex vivo experiments

1. Tissue sample preparation

Brain tumor samples were obtained from resected intra-operative tissue specimens. A representative portion of the tumor tissues from surgical excision was submitted for histopathologic evaluation, and the corresponding portion was preserved in 10% neutral buffered formalin until histopathological confirmation. The samples were collected for the study following informed consent from the patient/close relatives, and the study was approved by Institute Ethics Committee (Ethical clearance document No. NIMHANS/23rd (BS & NS DIV.)/2020). Histologically confirmed cases of Glioblastoma were utilized for the study ($n = 11$). Eleven cases that satisfied the inclusion criteria were recruited for the study (all male, 30–54 years age, parietal region = 6, frontal region = 5). For controls, age matched and location matched brain tissues ($n = 11$, all male, 35–55 years age, parietal region = 6, frontal region = 5) were procured from the Human Brain Tissue Repository (Brain bank) at the National Institute of Mental Health & Neurosciences (NIMHANS), sourced from postmortem of patients succumbing to road traffic accidents. All tissues were collected within 24 h post-mortem and fixed in 10% neutral buffered formalin (similar to brain tumor tissues).^{32,33} These samples were acquired with informed consent from close relatives and Ethical clearance from IEC (Ethical clearance document no. NIMHANS/IEC (BS & NS DIV.) 26th MEETING/2020-21). From the tissues, formalin-fixed tissue blocks (3–7 mm thickness, 15–30 mm length and breadth) were used for the study. Subsequently, the tumor and normal samples were characterized with ultrasound within two months post-fixation.

2. Tissue embedding in phantoms

To prepare the *ex vivo* brain tissue samples for acoustic analysis, a standardized procedure was followed to embed each sample in an agarose phantom. First, agarose (2% w/v, J66369-22, Thermo Fisher Scientific, Mumbai, India) was dissolved in de-ionized (MilliQ) water using a 700 W standard microwave oven (NN-ST266B FDG, Panasonic, Madhya Pradesh, India) by heating the solution in 30-s intervals. The resulting agarose solution was degassed in an ultrasonic sonication bath at 50 °C for 30 min. Subsequently, the solution was poured into a mold until half of the mold’s volume (82 mm × 56 mm × 25 mm) and left to solidify at room temperature (25 °C). The tissue sample was placed carefully above the agarose gel. The remaining agarose solution was cooled to a temperature of 35 to 40 °C, poured over the tissue sample, and allowed to solidify. The height of the top agarose layer was adjusted to be 6 mm above the tissue sample to ensure that the imaging focus was at the center of the sample.

3. Data acquisition

A standoff with degassed, de-ionized water was positioned above the phantom to facilitate acoustic propagation. RF data were acquired at five independent imaging planes for each tissue sample using a Vantage 128 system (Verasonics, Kirkland, WA) equipped with a linear array (L11-5v, center frequency of 7.6 MHz, Verasonics). The linear array was focused at a depth of 14 mm, which was within the tissue sample. The transducer was placed such that multiple reflections from the water and phantom interfaces were not within the imaging field of view and were minimized by placing an acoustic absorber beneath the phantom [Fig. 4(a)].

4. Attenuation compensation

Frequency-dependent attenuation coefficients were calculated using the broadband, insertion-loss, pulse-echo attenuation method [Fig. 4(b)].³⁴ The attenuation coefficients of the brain tissues were then determined by subtracting the attenuation coefficients of the reference agarose

phantom from the measured values. Each RF line was compensated for the acoustic attenuation of the brain tissues.

5. H-scan imaging

For each RF line, the 64-convolution H-scan algorithm was used by employing energy-normalized GH filters of even orders ranging from 2 to 128. These filters spanned the usable bandwidth of the linear array, i.e., 5–12 MHz. The GH₂ filter had a peak frequency of 5 MHz, while the GH₁₂₈ filter had a peak frequency of 12 MHz. Pseudo-coloring was then applied based on the order of the best-matched, maximum-correlated filter at each pixel. The IWPR was computed for every pixel within the sample region of interest (ROI). MATLAB was used for all post-processing tasks.

D. Statistical analysis

For the simulations, two-segment linear regression of the MIRC and IWPR measurements were performed for the NSPs with monodispersed scatterer distribution. The inflection points of the linear fits were defined as the maximum scatterer diameter in which the MIRC and IWPR parameters can be used to differentiate scatterer diameters at each concentration. A simple linear regression was performed for the bimodal scatterer simulation. For the simulations, the standard deviation (SD) of the H-scan parameters was computed for 10 independent realizations in the case of each monodisperse distribution and 5 independent realizations for each bimodal distribution. The goodness of fit was based on the root mean squared error (RMSE). The mean and standard error of the mean (SEM) of the IWPR parameter was computed for the normal and glioblastoma brain tissues (n = 11 samples per group and five imaging planes for each sample). The Anderson-Darling test was used to verify that the data sets of the IWPR estimates were normally distributed. The two-sample F-test was used to determine whether the data for the normal and glioblastoma samples had equal or unequal variances. The independent two-tailed t-test was used to determine whether the differences in IWPR estimates between normal and glioblastoma tissue samples were statistically significant. Statistical tests were performed using MATLAB and GraphPad Prism 9.5.1 (GraphPad

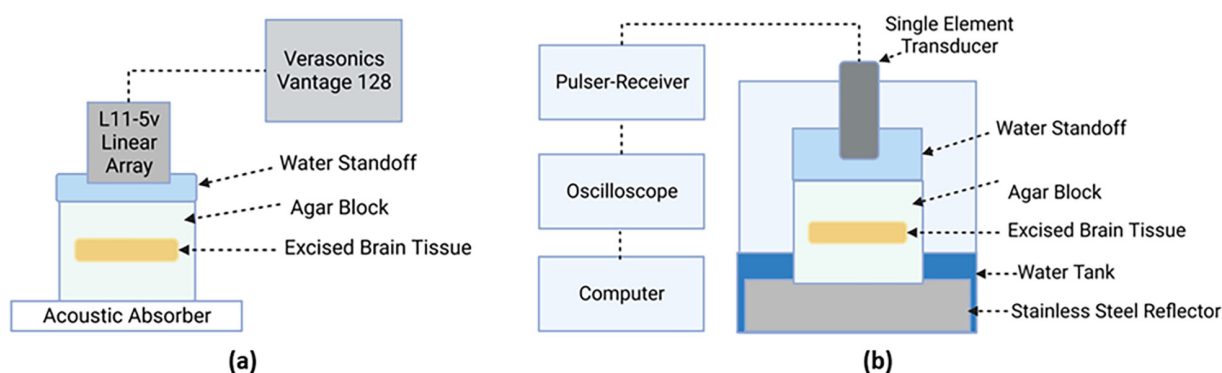


FIG. 4. (Color online) (a) Schematic of the imaging setup. (b) Pulse-echo attenuation measurement setup.

Software, Boston, MA). A p -value of less than 0.05 was considered statistically significant.

III. RESULTS

A. Simulations

For monodisperse NSPs, the two-segment linear regression analysis of the MIRC and IWPR estimates revealed differences in the inflection points [Figs. 5(a) and 5(b)]. Specifically, the inflection points for the MIRC estimates ranged from $62 \pm 2.6 \mu\text{m}$ at 0.2% w/v to $69 \pm 1.9 \mu\text{m}$ at 1.0% w/v (Table I); whereas, those of the IWPR estimates ranged from $120 \pm 7.2 \mu\text{m}$ at 0.2% w/v to $131 \pm 3.2 \mu\text{m}$ at 1.0% w/v, indicating that IWPR is sensitive to a broader range of scatterer diameters. The inflection point generally increases with concentration, suggesting a positive relationship with both the MIRC and IWPR H-scan parameters. However, the changes in the inflection points are relatively small, i.e., $62\text{--}69 \mu\text{m}$ and $120\text{--}131 \mu\text{m}$ for MIRC and IWPR, respectively.

The positive slope of the MIRC increased with increasing concentration, from 0.78 ± 0.041 at 0.2% w/v to 1.3 ± 0.041 at 1.0% w/v [Fig. 5(a)]. Whereas, for IWPR, the positive slope varied slightly across the concentrations [Fig. 5(b)] without a clear trend, demonstrating concentration independence. In Fig. 5(c), linear regression analysis of the IWPR for the bimodal distribution of 50 and 90 μm scatterers revealed that the trends at all concentrations overlap,

which indicates concentration independence. The positive slope shows the sensitivity of IWPR to changes in the bimodal distribution of scatterers. The RMSE also remained low and relatively stable (ranging from 0.081 to 0.15) across all concentrations, indicating consistent fit quality for all the regressions.

B. Ex vivo experiments

1. Histopathology

Representative histopathology images of normal and glioblastoma samples are shown in Fig. 6. Normal gray matter and white matter are shown in Figs. 6(a) and 6(b). Figure 6(c) shows a sample with tumor and necrosis regions. Samples graded as 100% tumor and tumor regions with leptomeningeal scars are shown in Figs. 6(d) and 6(e), respectively. Tumor samples showed infiltrating high-grade glioma with varying proportions of infiltrating neoplastic astrocytes, necrosis, and vascular stromal component.

2. H-scan imaging

Representative B-mode images of *ex vivo* brain tissues are shown in Figs. 7(a) and 7(b). The bright horizontal lines in the B-mode images represent specular reflections from the tissue-phantom interfaces. Figures 7(c) and 7(d) shows the H-scan images of the brain samples. Without attenuation compensation, the IWPR estimates were significantly different ($p < 0.0001$) between the normal brain and glioblastoma tissue

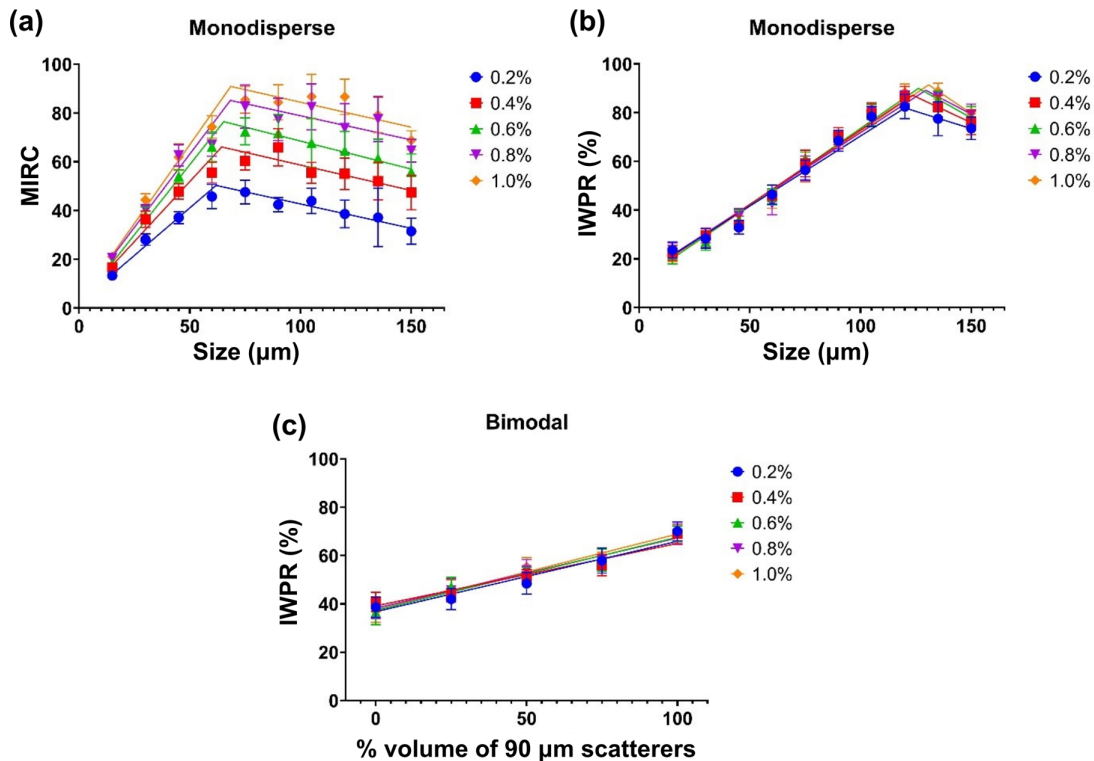


FIG. 5. (Color online) (a) Mean intensity of red channel (MIRC) estimates from the 2-convolution H-scan imaging of monodisperse NSPs with different scatterer diameters and concentrations. Intensity-weighted percentage of red (IWPR) estimates from the 64-convolution H-scan imaging for (b) monodisperse and (c) bimodal scatterer distributions with varying scatterer concentration. In (c), the IWPR is plotted against the % volume of 90 μm scatterers. Error bars represent the standard deviation of estimates.

TABLE I. Best-fit coefficients of two-segment linear regression and simple linear regression for monodisperse and bimodal distribution, respectively. Mean (SD) are shown.

		0.2% w/v	0.4% w/v	0.6% w/v	0.8% w/v	1.0% w/v
MIRC monodisperse	Slope	0.78 (0.041)	0.98 (0.042)	1.1 (0.042)	1.2 (0.048)	1.3 (0.041)
	Inflection point (μm)	62 (2.6)	64 (2.2)	65 (2.0)	68 (2.4)	69 (1.9)
	RMSE	0.15	0.12	0.11	0.11	0.092
IWPR monodisperse	Slope	0.58 (0.017)	0.61 (0.015)	0.63 (0.016)	0.59 (0.015)	0.62 (0.015)
	Inflection point (μm)	120 (7.2)	123 (4.9)	126 (4.3)	129 (3.9)	131 (3.2)
	RMSE	0.11	0.098	0.10	0.099	0.097
IWPR bimodal	Slope	0.29 (0.020)	0.26 (0.017)	0.30 (0.019)	0.29 (0.018)	0.31 (0.018)
	RMSE	0.10	0.081	0.091	0.084	0.085

samples ($43.0 \pm 1.0\%$ versus $34.9 \pm 0.61\%$, respectively; $p < 0.0001$). Acoustic attenuation compensation did not change the IWPR values appreciably; the respective values for normal and glioblastoma tissue were $44.1 \pm 1.4\%$ versus $36.2 \pm 0.65\%$ ($p < 0.0001$) (Fig. 8). There was only a 2.5% difference in mean IWPR estimates with and without attenuation compensation for normal tissues and a 3.7% difference for glioblastoma tissues. Of note, these images were collected from a small sample thickness (3 to 7 mm), which did not induce substantial attenuation spectrum shifts. When this technique is implemented during intraoperative surgeries in the future, it is envisaged to be performed using a probe which will be placed in close proximity to the tumor. Therefore, the confounding effects due to attenuation will be limited.

IV. DISCUSSION

The simulated results obtained from this study indicated that the IWPR parameter could assess a broader range of scatterer diameters compared to the MIRC parameter (Fig. 5 and Table I). The inflection point in Fig. 5 could be potentially explained by scattering theory, wherein the spherical Bessel function of the first kind of order 1 exhibits a first

peak around $ka = 1$.³⁵ If a simulation is obtained for 3-D spheres, it is plausible that we would obtain a first inflection point at the appropriate combination of size and frequency, which could help explain the inflection point observed in Fig. 5. Further investigation with (computationally intensive) 3-D simulations may provide more insight into this phenomenon. We will consider such theories with more realistic 3-D simulation setups in our future investigations to gain a comprehensive understanding of the underlying physics.

IWPR was demonstrated to be independent of scatterer concentration and sensitivity to changes in the bimodal scatterer distribution, which can be further applied to poly-disperse scatterer distributions. Thus, the IWPR is a diameter-dependent H-scan imaging parameter that can be useful for visualizing pathological changes in tissues based on changes in only scatterer diameters and not in scatterer concentrations. Although our study showed that H-scan derived estimates are independent of scatterer diameter, this trend may not hold at very high scatterer concentrations. At such high concentrations, multiple scattering effects can dominate. Further, at high concentrations, scatterers may form clusters or aggregates, effectively behaving as a single

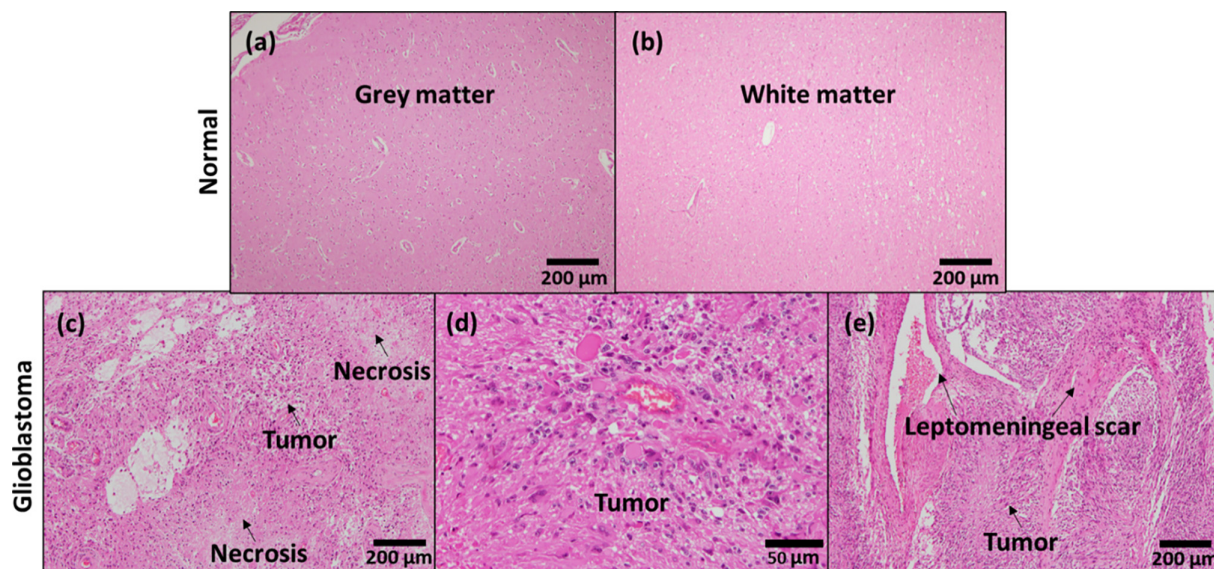


FIG. 6. (Color online) Representative histopathology images of (a) normal cortex with gray matter and (b) white matter, and glioblastoma brain tissue samples with (c) regions of tumor and necrosis, (d) 100% tumor, and (e) tumor with leptomenigeal scar. (H&E stain; magnification = scale bar.)

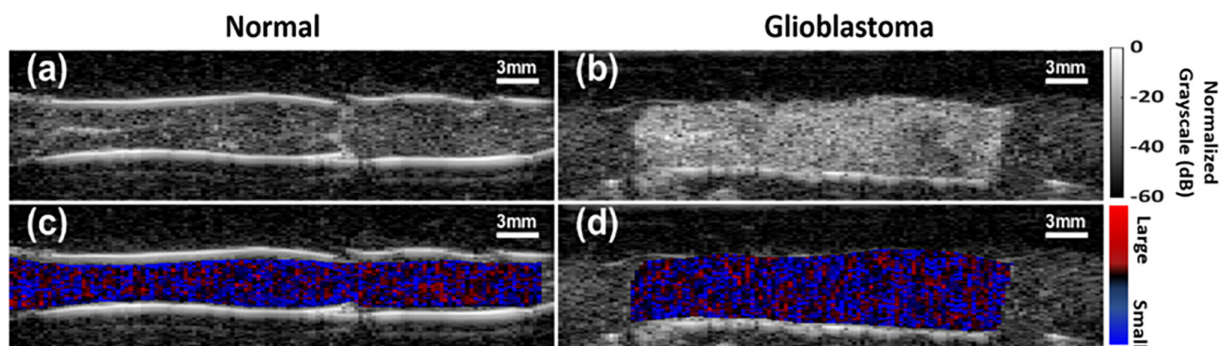


FIG. 7. (Color online) B-mode images (a), (b) and H-scan (c), (d) overlaid onto the B-mode images of normal [(a), (c)] and glioblastoma [(b), (d)] brain tissue samples.

large scatterer rather than individual, isolated scatterers. The effect of aggregation was not the goal of the current study but can be explored in future studies.

Notably, H-scan imaging allows tissue differentiation based on scatterers smaller than the resolution limit. In our simulations, we investigated a scatterer diameter range between 15 and 150 μm in diameter, which was below the resolution limit of our imaging system—the axial and lateral resolution (-6dB) were 300 and 600 μm , respectively. Our findings demonstrate the capability of H-scan imaging to detect and spatially visualize relative differences between scatterer diameters that are smaller than the imaging system’s resolution limit.

We used the GH_4 pulse in our simulations and experiments. Recent papers on H-scan imaging have employed Gaussian pulses due to their relative simplicity relative to Gaussian-weighted Hermite polynomials. Notably, the actual pulse generated from transducer excitation may not be appreciably different from a Gaussian pulse. Thus, the results obtained with GH_4 pulses may not exhibit substantial differences compared to the use of a simple Gaussian pulse, as previously reported in Ref. 4.

We observed that H-scan imaging of glioblastoma samples had less red component compared to normal brain tissue (Figs. 7 and 8). Although there is a lack of previous studies on brain tumors, these trends are similar to those

observed in previous studies on breast, pancreas, and thyroid malignancies.^{11,12,14–17} H-scan imaging of breast and thyroid tumors has shown that malignant tumors typically have less red intensity than benign lesions.^{14–16} Moreover, H-scan images of pancreatic tumors have shown that the red intensity is inversely correlated with the stage of cancer.^{11,12} The less red or more blue hue in H-scan images of malignant tumors suggest smaller scatterers due to the dense aggregate of tumor cells, which are characterized by a higher nuclear-cytoplasmic ratio than normal cells. Glioblastoma, a highly malignant tumor, is cellular, composed of cells that cluster together compared to normal brain tissue. In addition to the tumor cells, glioblastoma also displays areas of necrosis, vascular proliferation, stromal alterations, and fibrosis, which may influence the differences in spectral properties of tumor and normal brain tissue.

Another study has shown that the red intensity in H-scan images increases in malignant breast tumors with an increasing number of chemotherapy sessions.¹⁷ On the contrary, Diczno *et al.* have reported a decrease in the acoustic scatter diameter of breast tumors using quantitative ultrasound techniques in response to chemotherapy.³⁶ This apparent discrepancy may be due to changes in the stroma and morphology, induced by chemotherapy.¹⁷ Further studies with both H-scan and QUS imaging and detailed histopathological correlation may help ascertain these differences.

Unlike quantitative ultrasound (QUS) techniques, H-scan imaging is a qualitative approach for soft tissue characterization.^{37–39} However, the main advantage for H-scan is that it can display the relative differences in diameters of acoustic scatterers between tissue regions at higher spatial resolution than the kernel-based QUS methods. This capability can be useful for ensuring optimal delineation of brain tumor margins and safe resection of tumors, wherein the amount of brain tissue removed is critical.

In this study, formalin-fixed tissue samples were assumed to have similar microstructure as living tissues, which may be a reasonable assumption given that histology also employs fixation primarily for excellent preservation of cellular architecture that closely reflects *in vivo* tissue characteristics, essential for diagnosis. While fixation alters tissue hardness, it preserves cellular structure optimally aiding

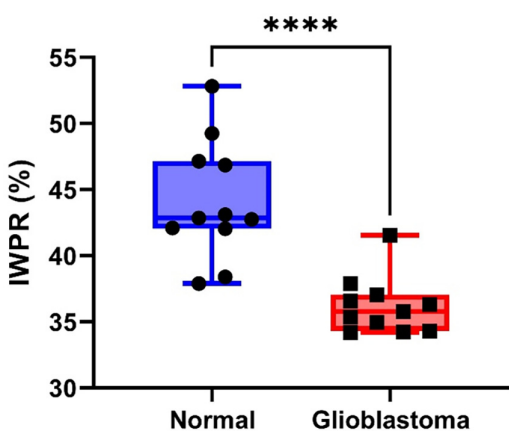


FIG. 8. (Color online) Intensity-weighted percentage red (IWPR) of normal brain and glioblastoma tissue samples. **** $p < 0.0001$.

in cellular characteristic identification on light microscopy. Adjacent normal brain tissue from the same subject with glioblastoma could not be obtained, as its against surgical practice, which made it challenging to evaluate the efficacy of this approach for tumor margin assessment. Further studies on a larger sample size will be essential to fully understand and attempt point to point correlation of H-scan imaging of alterations of microstructure at the tissue level.

A limitation of our simulation study was that the acoustic impedance was considered equal for all the NSPs. Further, the scatterers simulated in this study had moderate scattering strengths and were not weak. Such scatterers have been used previously for *in vitro* H-scan imaging studies.^{26–28} The varying acoustic impedance of each scatterer on the concentration independence of IWPR needs to be assessed in the future. Another limitation is that our work was also based on 2-D simulations because of computational considerations. Although 2-D simulations can provide a good approximation, we plan to incorporate a 3-D simulation setup in our future investigations to gain a comprehensive understanding of the underlying physics and comparative scattering theories. Nonetheless, the findings of this study set the groundwork for subsequent *in vivo* studies. Attenuation compensation based on image analysis,^{4,40} rather than measurements of the pulse-echo attenuation method, may be necessary to translate this approach. However, our IWPR results indicate that attenuation compensation may not be necessary when the tissue of interest is superficial.

V. CONCLUSION

The results emphasize the advantages of using IWPR as an effective H-scan imaging parameter for analyzing scatterer diameter distributions. The IWPR offers a broader range of sensitivity compared to the MIRC parameter and remains independent of the scatterer concentration. Additionally, IWPR exhibits reliable performance in the presence of bimodal scatterer distributions, making it a robust tool for various tissue scattering conditions. The simulation results were supported by *ex vivo* experiments on glioblastoma and normal brain tissues. The results revealed significant differences in IWPR estimates between the two tissue types, demonstrating the effectiveness of IWPR in distinguishing between brain tumor and normal tissues, highlighting its potential as a tool for tissue characterization and diagnosis.

ACKNOWLEDGMENTS

This work was supported by the Department of Science and Technology, Government of India (Grant No. DST/TDT/BDTD/08/2021).

AUTHOR DECLARATIONS

Conflict of Interest

The authors declare that they have no conflicts of interest to disclose.

Ethics Approval

Ethics approvals for the *ex vivo* brain tissue samples were obtained from the National Institute of Mental Health and Neuroscience through protocol Nos. NIMHANS/23rd (BS & NS DIV.)/2020 and NIMHANS/IEC (BS & NS DIV.) 26th MEETING/2020-21.

DATA AVAILABILITY

Data will be available upon reasonable request.

- ¹C. Fuller, “A little piece of mind: Best practices for brain tumor intraoperative consultation,” *Mod. Pathol.* **32**, 44–57 (2019).
- ²Z. Z. Zhang, L. B. E. Shields, D. A. Sun, Y. P. Zhang, M. A. Hunt, and C. B. Shields, “The art of intraoperative glioma identification,” *Front. Oncol.* **5**, 175 (2015).
- ³K. J. Parker, “Scattering and reflection identification in H-scan images,” *Phys. Med. Biol.* **61**, L20–L28 (2016).
- ⁴K. J. Parker and J. Baek, “Fine-tuning the H-scan for discriminating changes in tissue scatterers,” *Biomed. Phys. Eng. Express* **6**, 045012 (2020).
- ⁵F. L. Lizzi, M. Astor, E. J. Feleppa, M. Shao, and A. Kalisz, “Statistical framework for ultrasonic spectral parameter imaging,” *Ultrasound Med. Biol.* **23**, 1371–1382 (1997).
- ⁶M. L. Oelze and J. Mamou, “Review of quantitative ultrasound: Envelope statistics and backscatter coefficient imaging and contributions to diagnostic ultrasound,” *IEEE Trans. Ultrason. Ferroelectr. Freq. Control* **63**, 336–351 (2016).
- ⁷G. Cloutier, F. Destrempes, F. Yu, and A. Tang, “Quantitative ultrasound imaging of soft biological tissues: A primer for radiologists and medical physicists,” *Insights Imag.* **12**, 127 (2021).
- ⁸M. F. Insana, T. J. Hall, and L. T. Cook, “Backscatter coefficient estimation using array transducers,” *IEEE Trans. Ultrason. Ferroelectr. Freq. Control* **41**, 714–723 (1994).
- ⁹Y. Kurokawa, H. Taki, S. Yashiro, K. Nagasawa, Y. Ishigaki, and H. Kanai, “Estimation of size of red blood cell aggregates using backscattering property of high-frequency ultrasound: *In vivo* evaluation,” *Jpn. J. Appl. Phys.* **55**, 07KF12 (2016).
- ¹⁰Q. Shenming, L. Xiang, and G. Zhihua, “A new hyperspectral image classification method based on spatial-spectral features,” *Sci. Rep.* **12**, 1541 (2022).
- ¹¹J. Baek, R. Ahmed, J. Ye, S. A. Gerber, K. J. Parker, and M. M. Doyley, “H-scan, shear wave and bioluminescent assessment of the progression of pancreatic cancer metastases in the liver,” *Ultrasound Med. Biol.* **46**, 3369–3378 (2020).
- ¹²J. Baek and K. J. Parker, “H-scan trajectories indicate the progression of specific diseases,” *Med. Phys.* **48**, 5047–5058 (2021).
- ¹³M. Khairalseed, K. Javed, G. Jashkaran, J.-W. Kim, K. J. Parker, and K. Hoyt, “Monitoring early breast cancer response to neoadjuvant therapy using h-scan ultrasound imaging: Preliminary preclinical results,” *J. Ultrasound Med.* **38**, 1259–1268 (2019).
- ¹⁴M. Khairalseed, R. Laimes, J. Pinto, J. Guerrero, H. Chavez, C. Salazar, G. R. Ge, K. J. Parker, R. J. Lavarello, and K. Hoyt, “Classification of thyroid nodules in H-scan ultrasound images using texture and principal component analysis,” in *2021 IEEE UFFC Latin America Ultrasonics Symposium (LAUS)* (IEEE, Piscataway, NJ, 2021), pp. 1–4.
- ¹⁵M. Khairalseed, R. Laimes, J. Pinto, J. Guerrero, H. Chavez, C. Salazar, G. R. Ge, R. J. Lavarello, and K. Hoyt, “H-Scan ultrasound imaging for the classification of thyroid tumors,” in *2022 IEEE International Ultrasonics Symposium (IUS)* (IEEE, Piscataway, NJ, 2022), pp. 1–3.
- ¹⁶Y. Ouyang, P.-H. Tsui, S. Wu, W. Wu, and Z. Zhou, “Classification of benign and malignant breast tumors using H-scan ultrasound imaging,” *Diagnostics* **9**, 182 (2019).
- ¹⁷H. Piotrkowska-Wroblewska, K. Dobruch-Sobczak, M. Gumowska, and J. Litniewski, “Changes in quantitative ultrasound imaging as the predictor of response to neoadjuvant chemotherapy in patients with breast cancer,” in *2022 IEEE International Ultrasonics Symposium (IUS)* (IEEE, Piscataway, NJ, 2022), pp. 1–4.

- ¹⁸H. Tai, R. Margolis, J. Li, and K. Hoyt, "H-scan ultrasound monitoring of breast cancer response to chemotherapy and validation with diffusion-weighted magnetic resonance imaging," *J. Ultrasound Med.* **42**, 1297–1306 (2023).
- ¹⁹H. Tai, J. Song, J. Li, S. Reddy, M. Khairalseed, and K. Hoyt, "Three-dimensional H-scan ultrasound imaging of early breast cancer response to neoadjuvant therapy in a murine model," *Invest. Radiol.* **57**, 222–232 (2022).
- ²⁰J. Baek, A. M. O'Connell, and K. J. Parker, "Breast lesion detection and visualization utilizing artificial intelligence and the H-scan," in *2022 IEEE International Ultrasonics Symposium (IUS)* (IEEE, Piscataway, NJ, 2022), pp. 1–4.
- ²¹G. R. Ge, R. Laimes, J. Pinto, J. Guerrero, H. Chavez, C. Salazar, R. J. Lavarello, and K. J. Parker, "H-scan analysis of thyroid lesions," *J. Med. Imag.* **5**(1) 013505 (2018).
- ²²J. Baek, S. S. Qin, P. A. Prieto, and K. J. Parker, "H-scan imaging and quantitative measurement to distinguish melanoma metastasis," in *2021 IEEE International Ultrasonics Symposium (IUS)* (IEEE, Piscataway, NJ, 2021), pp. 1–4.
- ²³C. M. Rumack and D. Levine, *Diagnostic Ultrasound* (Elsevier Health Sciences, New York, 2017).
- ²⁴B. E. Treeby, J. Jaros, A. P. Rendell, and B. T. Cox, "Modeling nonlinear ultrasound propagation in heterogeneous media with power law absorption using a k-space pseudospectral method," *J. Acoust. Soc. Am.* **131**, 4324–4336 (2012).
- ²⁵A. D. Poularikas, *Transforms and Applications Handbook* (CRC Press, Boca Raton, FL, 2018).
- ²⁶M. Khairalseed, K. Brown, K. J. Parker, and K. Hoyt, "Real-time H-scan ultrasound imaging using a Verasonics research scanner," *Ultrasonics* **94**, 28–36 (2019).
- ²⁷M. Khairalseed, K. Hoyt, J. Ormachea, A. Terrazas, and K. J. Parker, "H-scan sensitivity to scattering size," *J. Med. Imag.* **4**(4), 043501 (2017).
- ²⁸M. Khairalseed, F. Xiong, J.-W. Kim, R. F. Mattrey, K. J. Parker, and K. Hoyt, "Spatial angular compounding technique for H-scan ultrasound imaging," *Ultrason Med. Biol.* **44**, 267–277 (2018).
- ²⁹J. Baek, E. Hysi, X. He, D. A. Yuen, M. C. Kolios, and K. J. Parker, in "Detecting kidney fibrosis using H-scan," *2022 IEEE International Ultrasonics Symposium (IUS)* (IEEE, Piscataway, NJ, 2022), pp. 1–3.
- ³⁰J. Baek, S. S. Poul, T. A. Swanson, T. Tuthill, and K. J. Parker, "Scattering signatures of normal versus abnormal livers with support vector machine classification," *Ultrason Med. Biol.* **46**, 3379–3392 (2020).
- ³¹J. Baek, T. A. Swanson, T. Tuthill, and K. J. Parker, "Support vector machine (SVM) based liver classification: Fibrosis, steatosis, and inflammation," in *2020 IEEE International Ultrasonics Symposium (IUS)* (IEEE, Piscataway, NJ, 2020), pp. 1–4.
- ³²B. S. Arjun, B. Alekya, R. S. Hari, V. Vikas, A. Mahadevan, and H. J. Pandya, "Electromechanical characterization of human brain tissues: A potential biomarker for tumor delineation," *IEEE Trans. Biomed. Eng.* **69**, 3484–3493 (2022).
- ³³A. D. Stan, S. Ghose, X.-M. Gao, R. C. Roberts, K. Lewis-Amezcuca, K. J. Hatanpaa, and C. A. Tamminga, "Human postmortem tissue: What quality markers matter?," *Brain Res.* **1123**, 1–11 (2006).
- ³⁴A. Ruland, J. M. Hill, and G. G. Wallace, "Reference phantom method for ultrasonic imaging of thin dynamic constructs," *Ultrason Med. Biol.* **47**, 2388–2403 (2021).
- ³⁵M. F. Insana, R. F. Wagner, D. G. Brown, and T. J. Hall, "Describing small-scale structure in random media using pulse-echo ultrasound," *J. Acoust. Soc. Am.* **87**, 179–192 (1990).
- ³⁶D. DiCenzo, K. Quiaoit, K. Fatima, D. Bhardwaj, L. Sannachi, M. Gangeh, A. Sadeghi-Naini, A. Dasgupta, M. C. Kolios, M. Trudeau, S. Gandhi, A. Eisen, F. Wright, N. L. Hong, A. Sahgal, G. Staniszc, C. Brezden, R. Dinniwell, W. T. Tran, W. Yang, B. Curpen, and G. J. Czarnota, "Quantitative ultrasound radiomics in predicting response to neoadjuvant chemotherapy in patients with locally advanced breast cancer: Results from multi-institutional study," *Cancer Med.* **9**, 5798–5806 (2020).
- ³⁷R. J. Lavarello, W. R. Ridgway, S. S. Sarwate, and M. L. Oelze, "Characterization of thyroid cancer in mouse models using high-frequency quantitative ultrasound techniques," *Ultrason Med. Biol.* **39**, 2333–2341 (2013).
- ³⁸M. L. Montero, O. Zenteno, B. Castaneda, M. Oelze, and R. Lavarello, "Evaluation of classification strategies using quantitative ultrasound markers and a thyroid cancer rodent model," in *2014 IEEE International Ultrasonics Symposium* (IEEE, Piscataway, NJ, 2014), pp. 1916–1919.
- ³⁹H. Tadayyon, A. Sadeghi-Naini, L. Wirtzfeld, F. C. Wright, and G. Czarnota, "Quantitative ultrasound characterization of locally advanced breast cancer by estimation of its scatterer properties," *Med. Phys.* **41**, 012903 (2014).
- ⁴⁰H. Tai, M. Khairalseed, and K. Hoyt, "Adaptive attenuation correction during H-scan ultrasound imaging using K-means clustering," *Ultrasonics* **102**, 105987 (2020).